Aalborg Universitet

An Enhanced Dual Droop Control Scheme for Resilient Active Power Sharing among Paralleled Two-Stage Converters

Liu, Hongpeng; Yang, Yongheng; Wang, Xiongfei; Loh, Poh Chiang; Blaabjerg, Frede; Wang, Wei; Xu, Dianguo

Link to publication from Aalborg University

An Enhanced Dual Droop Control Scheme for Resilient Active Power Sharing among Paralleled Two-Stage Converters

Hongpeng Liu, *Member, IEEE*, Yongheng Yang, *Member, IEEE*, Xiongfei Wang, *Member, IEEE*,
Poh Chiang Loh, Frede Blaabjerg, *Fellow, IEEE*, Wei Wang, *Member, IEEE*,
and Dianguo Xu, *Senior Member, IEEE*

Abstract—**Traditional droop-controlled system has assumed that generators can always generate the powers demanded from them. This is true with conventional sources, where fuel supplies are usually planned in advance. For renewable sources, it may also be possible if energy storage is available. Energy storage, usually as batteries, may however be expensive, depending on its planned capacity. Renewable sources are therefore sometimes installed as non-dispatch-able sources without storage. This may not be viable for remote grids, where renewable sources may be the only or major type of sources. In those cases, traditional droop scheme may not work well when its demanded power cannot be met by some renewable sources due to intermittency. When that happens, the system may become unstable with some sources progressively brought out of generation. To avoid such occurrence, an enhanced dual droop scheme is proposed for general two-stage converters with front rectifiers or dc-dc converters for conditioning powers from renewable sources and rear inverters for channeling powers to remote grids. Unlike the traditional droop scheme, the proposed dual droop scheme uses both dc-link voltage and generated powers for determining the required control actions, which have subsequently been proven stable by small-signal analysis. Experimental results have also verified the effectiveness of the dual droop scheme.**

Index Terms—**Microgrid, two-stage converters, droop control, active power sharing, small-signal analysis.**

I. INTRODUCTION

With growing concern of the environment and cost of energy, renewable energy sources (RESs) have increasingly been deployed as distributed generators (DGs) in microgrids (MGs) or remote grids, where laying of transmission lines may be expensive and transportation of fuels may be inconvenient [1]-[4]. RESs are therefore prospective alternatives even though they are not likely to fully replace conventional generators. Their penetration has hence grown rapidly with wind, tidal and photovoltaic (PV) sources being the most popular because of their abundance, cleanness and comparatively low production cost [5]-[8]. The number of RESs in shunt may also be high to meet greater load demand. Their parallel control has hence been the next target of interest.

One possibility is to try droop control mimicked from the parallel behaviors of multiple synchronous generators [9]-[12]. The droop-controlled converters can then share active and reactive powers proportionally based on their respective ratings. The droop scheme has however been analyzed with single-stage converters in most cases, which obviously, do not cover RESs with front rectifiers or dc-dc converters, and rear inverters [13]-[15]. The resulting converters are referred to as two-stage converters with many control freedoms available for enhancing the droop scheme, even though not widely explored at present.

Some examples can be found in [16]-[22], where the droop principle has been applied to multiple PV sources in a microgrid. Additionally, in [16] and [17], the transfer between grid-connected and islanded modes has been activated by a reconfiguration of controllers in a single PV source. This is subsequently found to be non-optimized when compared with schemes that use the same control structure in both modes. The droop concept from the Consortium for Electric Reliability Technology Solutions (CERTS) is then raised in [18], where PV inverters have been droop-controlled to keep the dc bus voltage stable during load transient, and automatically reduce generation during low-load islanding. The CERTS concept has however been investigated with only single-stage inverters.

Even more recent is the universal controller proposed in [20], where maximum power point tracking (MPPT), droop control and dc-link voltage regulation have been managed simultaneously without control reconfiguration. The controlled source can therefore participate in voltage and frequency regulations of the MG, while generating maximum power. The MG must in turn have other non-renewable sources or storage for balancing supply and demand, which if not catered, will severely limit variation range of the loads. Additionally, the absence of non-renewable sources or storage may introduce a

concern, which existing droop schemes have not encountered since they usually assume active power demanded by the droop controller can always be supplied by the sources [23]. This may not be true with RESs because of intermittency caused by climatic and environmental changes.

When that happens (powers demanded by droop controllers cannot be met by RESs), the constrained RESs will try to increase the system frequency, while the other RESs with enough capacities will try to lower frequency to fill energy shortfall in case of inductive connecting lines. Both groups of RESs are therefore in conflict with no common stable system frequency determined. The simplest solution is to add energy storage if the usual droop scheme is used without changes. Capacity of the storage may however be sizable if each RES is to meet its droop power command at all times. The total installed storage may therefore be expensive. To avoid such costs, the RESs can be made non-dispatch-able, but only when other dispatch-able sources are presented. Making them non-dispatch-able also does not meet the CERTS requirement mentioned in [18].

It may therefore be necessary for the RESs to remain as droop-controlled, but not with the existing droop scheme applied. Instead, the enhanced dual droop scheme proposed in this paper should be used, which as its name implies, uses two droop relationships for controlling each two-stage converter. Its principle is based on adaptively adjusting the droop lines in accordance to the load demand and ambient conditions detected by sensing the converter dc-link voltage and power generated. Since these quantities are already sensed for normal control purposes, the proposed scheme does not demanded for additional hardware, and can hence be easily retrofitted to existing RES converters. Experimental results obtained from two two-stage single-phase converters have readily verified the expectation in terms of resilient active power sharing even when subject to intermittency experienced by the RESs.

II. EXAMPLE SYSTEM

For illustration, the system shown in Fig. 1(a) is considered. It consists of two PV converters with each converter assembled by a front dc-dc boost converter and a rear dc-ac single-phase inverter, as shown in Fig. 1(b). Control scheme of the converter is also shown in the same figure. It should nonetheless be emphasized that other two-stage converters consisting of ac-dc rectifiers and dc-ac inverters found in wind generation can similarly be considered, if preferred, without altering the findings concluded. Considering only two RESs is also deemed as appropriate for studying intermittency, which when happened, always results in two lumped groups of RESs. The first group consists of those with active power deficiency, while the second group consists of those with enough capacity for continuous generation. An example system with two RESs for representing the two lumped groups is therefore sufficient for demonstrating intermittency, while preserving simplicity for easier understanding.

Returning to the individual two-stage converter shown in Fig. 1(b), its boost stage is controlled by a single-loop voltage controller notated as $G_B(s)$. Input to $G_B(s)$ is the difference
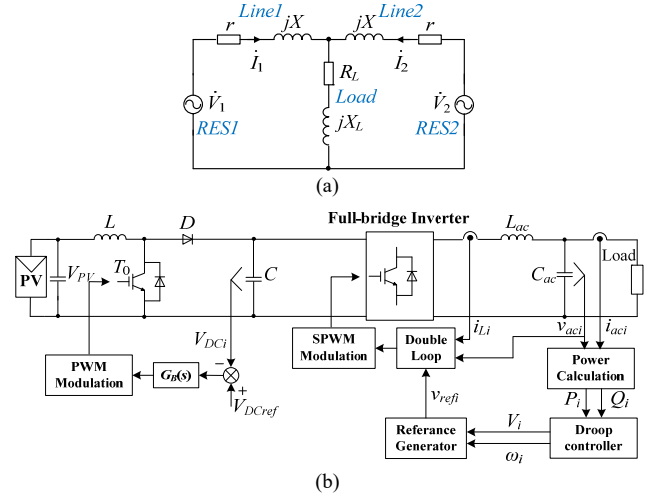
Fig. 1. Illustrations of (a) system with droop-controlled RESs, and (b) schematic within each RES converter.

between measured dc-link voltage V_{DCi} ($i = 1$ or 2 for the two RESs considered) and its reference V_{DCref}, which in theory, can be nullified by a Proportional-Integral (PI) $G_B(s)$ or any other controllers that can force a zero dc steady-state error. Control of the front boost stage is therefore comparatively easier than the rear inverter, whose output voltage v_{aci} and current i_{aci} must first be measured for computing P_i and Q_i. The computed powers can then be fed to conventional P-ω and Q-V droop expressions given in (1) and (2).

$$\omega_i = \omega_{0i} - k_{pi}(P_i - P_{0i}) \qquad (1)$$

$$V_i = V_{0i} - k_{qi}(Q_i - Q_{0i}) \qquad (2)$$

where ω_{0i} and V_{0i} are the rated angular frequency and output voltage amplitude of converter "i", P_{0i} and Q_{0i} are its rated active and reactive powers, and k_{pi} and k_{qi} are its active and reactive power droop coefficients, respectively.

The determined V_i and ω_i from (1) and (2) can eventually be used for forming the demanded voltage reference $v_{refi} = V_i\cos(\omega_i t)$ for tracking by the usual voltage and current controllers. The expressions in (1) and (2) are however for predominantly inductive connecting lines only. For predominantly resistive lines, the expressions change to those given in (3) and (4) [24], where definitions of the variables remain unchanged. The only differences noted are frequency is now determined by reactive power, while voltage magnitude is determined by active power. Such simple swopping of dependencies will however cause RESs controlled by (3) and (4) to behave differently from those controlled by (1) and (2) when subject to intermittency. These differences are analyzed in the next section, where an anticipated problem related to the traditional droop scheme has been explained.

$$\omega_i = \omega_{0i} + k_{qi}(Q_i - Q_{0i}) \qquad (3)$$

$$V_i = V_{0i} - k_{pi}(P_i - P_{0i}) \qquad (4)$$

III. ANTICIPATED PROBLEM

To explain the problem faced by the two droop-controlled RESs shown in Fig. 1(a), conditions collected in Fig. 2 are analyzed for the case of (1) and (2) used for regulating the two

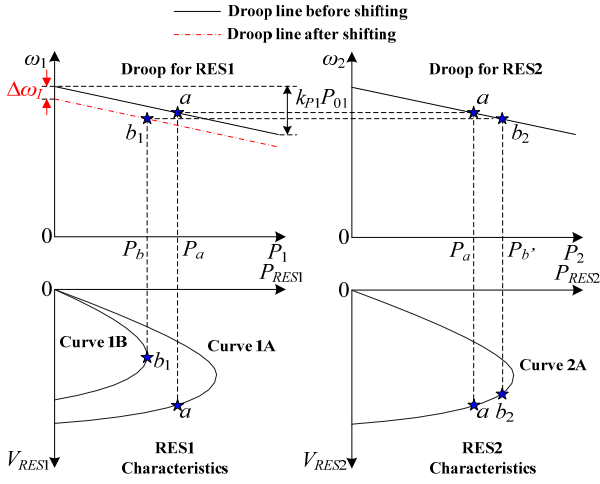Fig. 2. Inductive P-ω droop interactions with RES characteristic curves (same for resistive P-V interactions upon replacing ω with V).

RESs. For simplicity, the two RESs are also assumed as equally rated, which will nonetheless be true if they are normalized to the common per-unit range. They are therefore regulated by the same active and reactive droop lines with the same droop coefficients ($k_{p1} = k_{p2}$ and $k_{q1} = k_{q2}$), if the existing droop principle is applied. They are however assumed to be located differently, and hence subject to different ambient conditions including cloud passing that can occasionally cause solar irradiation to drop in case of a PV converter. It is therefore possible for the RESs to have different characteristic curves depending on their ambient conditions.

With the RES conditions clarified, Fig. 2 shows an instant where both RESs begin with the same characteristic curves 1A and 2A indicated at the bottom of Fig. 2. Their initial common droop lines will then mark out the same operating points, notated commonly as "a" (another operating point on the positive-sloping side of the PV curve will be addressed later). Their power generations and angular frequencies will thus be $P_1 = P_2 = P_a$ and $\omega_1 = \omega_2 = \omega_a$ with the latter naturally enforced by the network in the steady state. The characteristic curve of RES1 is next assumed to fall from curve 1A to curve 1B, such that its new maximum power P_b at "b_1" is lower than P_a marked by its droop line and initial characteristic curve 1A ($P_b < P_a$). RES1 is thus not able to provide the demanded droop power if the existing droop scheme is applied without modification. The droop scheme of RES1 will hence try to increase its frequency along the droop line to lower its droop active power command. At the same time, RES2 will attempt to lower its frequency to raise its generation to meet the load demand, which certainly, is possible if the maximum power of curve 2A is high enough. Both RESs are therefore in conflict with a common steady-state frequency and hence stability not readily achievable.

A straightforward solution is to add energy storage with usually oversized capacity to each RES, so that the combined RES-storage entity is capable of generating any amount of active power demanded by its droop line. Energy storage with sufficient capacity may however incur significant investment costs. To avoid or lower such costs, another possibility is to operate the RESs as non-dispatch-able sources, which is only possible if there are other dispatch-able sources for regulating the network voltage. In case where such dispatch-able sources are not present or not strong like in some remote MGs, the RESs must be operated as dispatch-able sources, which is also the recommendation mentioned by CERTS in [18]. When that happens (droop-controlled RESs), dc-link voltage V_{DC1} of RES1 with insufficient capacity will gradually collapse, since power delivered to the dc-link by the boost converter in Fig. 1(b) is less than power drawn out by the rear inverter. Eventually, only RES2 is left powering the loads or it will be tripped too if its capacity cannot meet the full load demand. This unstable situation may be avoided, if (1) and (2) are modified to keep both RESs in operation even though capacity of RES1 has dropped.

The same dropping of dc-link voltage V_{DC1} will occur too, when (3) and (4) are used for regulating the two RESs connected by predominantly resistive lines. The exception is overall collapsing of V_{DC1} of RES1 may not always happen, since ac voltages V_1 and V_2 of both RESs need not be exactly equal unlike frequencies ω_1 and ω_2. Therefore, when the characteristic curve of RES1 changes from curve 1A to curve 1B in Fig. 2, RES1 will still try to increase its voltage V_1 to lower its droop power command, while RES2 will still try to decrease its voltage V_2 to raise its generation. But, as soon as the lowered droop command of RES1 can be met by its reduced generation, its dc-link voltage V_{DC1} stabilizes and returns to its reference value V_{DCref}.

The shortfall in generation is then shouldered by RES2 if its capacity is sufficient. It should however be noted that such stabilization is possible only when the fall in capacity of RES1 is not sizable. Otherwise, the increase in V_1 and decrease in V_2 may cause a relatively higher voltage to appear across RES1, which in principle, may not be possible since RES1 is generating lesser power. Classical droop schemes represented by (1) and (2) or (3) and (4) are therefore not directly applicable to dispatch-able RESs in general.

IV. ENHANCED DUAL DROOP SCHEME

A. Inductive Connecting Lines

In Section III, the conflicting frequency excursion during capacity reduction of RES1 is explained. This excursion will eventually lead to system breakdown. To retain stability, it is therefore necessary to nullify such excursion by allowing the two RESs to decrease their frequencies together, while permitting RES1 to lower its droop power command and RES2 to raise its droop power command. One way to do it is to lower the original droop line of RES1 by $\Delta\omega_I$, seen from the top of Fig. 2, until the dashed vertical line drawn from "b_1" first touches the new characteristic curve 1B of RES1. Point "b_1" is then the new operating point, at which the reduced droop power command can be met by maximum power P_b generated by RES1. More importantly, point "b_1" is at a lower frequency needed by RES2 for increasing its generation from P_a to $P_{b'}$ at operating point "b_2". RES2 is thus able to compensate for any energy shortfall introduced by RES1 without experiencing conflicting frequency excursion.

The problem is determining the value of $\Delta\omega_I$, which the simplest way is to automatically generate it by feeding the power imbalance to a PI controller. Output of the PI controller can then be used as $\Delta\omega_I$, which in the steady state, will always enforce a zero power imbalance. The integral output is however indefinite with many solutions available for $\Delta\omega_I$ if the system includes more than one RES (the same reason why droop and not PI control is used for paralleled systems). It is therefore not encouraged to use the PI controller for generating $\Delta\omega_I$. Instead, the droop principle should be reapplied, where an input should be permitted to drop slightly for generating the uniquely mapped $\Delta\omega_I$. The input here can be chosen as the dc-link voltage V_{DCi} ($i = 1$ or 2), which instead of being regulated constant, is now permitted to fall slightly in the range of $V_{DCmin} \leq V_{DCi} \leq V_{DCref}$, whenever the droop power command cannot be met by the RES capacity.

The lower limit of the range V_{DCmin} should in fact be higher than the maximum inverter output voltage to avoid over-modulation. It should thus be determined from (2) as $V_{DCmin} \geq V_{0i}$, before writing the final droop expression for computing $\Delta\omega_I$ in (5), if the connecting lines are predominantly inductive.

$$\Delta\omega_I = \begin{cases} k_f \left(V_{DCi} - V_{DCref} \right), & V_{DCi} < V_{DCref} \\ 0, & V_{DCi} \geq V_{DCref} \end{cases} \tag{5}$$

$$-k_{pi}P_{0i} \leq \Delta\omega_I \leq 0$$

where k_f is the droop coefficient for calculating $\Delta\omega_I$. Some insights deduced from (5) can further be summarized as follows:

- Offset $\Delta\omega_I$ varies in the range given in (5), whose lower limit is obtained by subtracting maximum and minimum of (1) ($\omega_{0i} - (\omega_{0i} + k_{pi}P_{0i})$). The minimum permitted value at the left-hand side of (5) is thus $-k_{pi}P_{0i}$, while the minimum permitted value at its right-hand side is $k_f \left(V_{DCmin} - V_{DCref} \right)$. Matching them, an initial pre-tuned value for k_f can thus be determined as $k_{pi}P_{0i} / (V_{DCref} - V_{DCmin})$.

- The actual V_{DCi}, when fallen below V_{DCref}, represents a lack of RES capacity. The inverter droop power command must hence be lowered by adding a negative $\Delta\omega_I$.

- The actual V_{DCi}, when risen above V_{DCref}, represents an excess RES capacity. The demanded droop power can therefore be met without having to lower the droop line. No offset ($\Delta\omega_I = 0$) is thus needed.

- As V_{DCi} must now droop slightly, controller $G_B(s)$ for the boost converter in Fig. 1(b) cannot be a PI controller. It should instead be a proportional controller with a small gain given by $(V_{DCref} - V_{DCmin}) / P_{0i}$. Implementation of this gain is no different from those small droop coefficients found in (1) to (4). It will hence not cause additional inconvenience.

The proposed dual droop expression for active power regulation can eventually be expressed as (6), which in effect, is a combination of (1) and (5) for predominantly inductive lines. In contrast, droop expression for reactive power regulation remains unchanged as (2), since internal active power variation

Fig. 3. Improved dual droop scheme.

will not limit reactive power delivered by the rear inverter. The overall dual droop scheme is thus represented by Fig. 3 drawn using (2) and (6).

$$\omega_i = \underbrace{\omega_{0i} - k_{pi}(P_i - P_{0i})}_{} + \underbrace{k_f(V_{DCi} - V_{DCref})}_{} \tag{6}$$

B. Resistive Connecting Lines

The same conflicting excursion will happen when the two RESs are connected by resistive lines and governed by those traditional droop expressions given in (3) and (4). The only difference is that the conflict is triggered by diverting voltages rather than frequencies. The same dual droop scheme can therefore be used for computing ΔV_I needed for lowering the droop line of RES1 whenever its capacity reduces. The expression developed for ΔV_I is specifically given in (7), which no doubt, is similar to that in (5) for inductive connecting lines. The droop coefficient in (7) has however been re-notated as k_V for highlighting its voltage, rather than frequency, adjustment.

$$\Delta V_I = \begin{cases} k_V \left(V_{DCi} - V_{DCref} \right), & V_{DCi} < V_{DCref} \\ 0, & V_{DCi} \geq V_{DCref} \end{cases} \tag{7}$$

$$-k_{pi}P_{0i} \leq \Delta V_I \leq 0$$

The dual droop active power expression is then given in (8) with its first term used for power sharing like in (4) and its second term used for compensating RES capacity reduction. Expression for reactive power regulation however remains unchanged, and can still be represented by (3).

$$V_i = \underbrace{V_{0i} - k_{pi}(P_i - P_{0i})}_{} + \underbrace{k_V(V_{DCi} - V_{DCref})}_{} \tag{8}$$

C. Special Operating Point Identification

Returning to Fig. 2, an observation noted is all operating points marked are on the negative-sloping sides of the PV curves, rather than on their positive-sloping sides. To prove that this is indeed a stable case with the proposed dual droop scheme, the PV curve of RES1 with operating point "a" marked is redrawn in Fig. 4. As explained earlier, this operating point is determined by the droop-demanded power P_a, which flows through the rear dc-ac inverter in the steady state.

Assuming next that "a" is slightly perturbed and moved to "a_1" in Fig. 4(a), the PV harnessed power P_{a1} at "a_1" will

become higher than the droop-demanded power P_a. That causes the dc-link voltage V_{DC1} to rise slightly. From Fig. 1(b), a small negative error $(V_{DCref} - V_{DC1})$ is thus introduced, and fed to the positive gain $G_B(s)$ and modulation block. The modulation block, in turn, causes duty ratio of switch T_0 and its accompanied boost gain to decrease. The decrease in gain is mostly contributed by an increase in PV input voltage because of the usual sizable dc-link capacitance used. Operating point "a_1" will hence be brought back to "a" by the increase in PV voltage.

The same restoring effect will be triggered when "a" is perturbed to "a_{1a}", implying that "a" is a stable operating point, which RES1 will remain in the steady state. It should additionally be emphasized that "a" being a stable point is demonstrated with only the control scheme of the front boost converter mentioned. It is therefore valid regardless of whether the traditional or proposed droop scheme is used with the rear inverter. The two droop schemes will however behave differently when "c" is the assumed operating point, as marked in Fig. 4(b). Considering again that "c" is slightly perturbed to "c_1", the small negative error $(V_{DCref} - V_{DC1})$ introduced will cause the PV input voltage to rise as explained earlier. But, instead of returning to "c", the increase now causes "c_1" to deviate further until it reaches the stable operating point "a".

The reverse perturbation of "c" to "c_{1a}" can similarly be evaluated, which as anticipated, will introduce a small positive error $(V_{DCref} - V_{DC1})$ for raising duty ratio of switch T_0 and its boost gain. The increase in gain, in turn, causes the PV input voltage to lower and eventually collapse to zero, rather than returning to "c". This scenario will however occur only with the traditional droop scheme, whose droop power command for the rear inverter will be kept unchanged at P_a. In contrast, with the proposed dual droop scheme, the positive error $(V_{DCref} - V_{DC1})$ will gradually cause the droop power command of the inverter to drop from P_a to $P_{c'}$ in Fig. 4(b), which in most cases, is much slower since the droop scheme is located at the outermost loop of the usual three-loop structure.

This new $P_{c'}$ will also be smaller than P_{c1a} harnessed at "c_{1a}" because of the steeper droop gradient with respect to voltage than the positive-sloping side of the PV curve. The positive power flow $(P_{c1a} - P_{c'})$ through the dc-link capacitance will then gradually cause $(V_{DCref} - V_{DC1})$ to become negative, boost gain to drop, and "c_{1a}" to move to "a". Operating point "c" is therefore an unstable point, which upon slightly perturbed, will shift RES1 to stable point "a" in the steady state.

V. SMALL-SIGNAL ANALYSIS

To evaluate stability of the converters shown in Fig. 1(a), small-signal model of each converter is first developed based on (2) and (6), before models of the two converters are merged for representing the overall system (converter models derived using (3) and (8) are relatively similar, and hence not duplicated). Details of the derivation are presented as follows.

A. Model of Single Converter

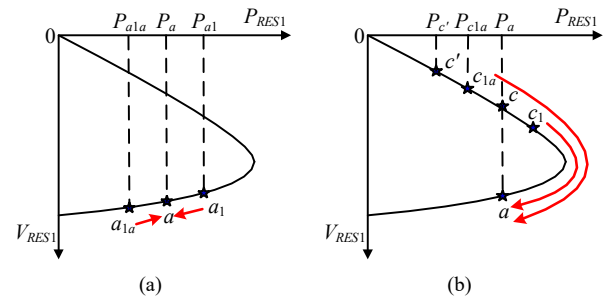As per usual, the droop process begins by computing the

Fig. 4. Perturbed operating point trajectories along (a) negative- and (b) positive-sloping sides of PV curve.

generated active and reactive powers of each converter using locally measured voltage and current quantities. The computed instantaneous powers $P_i(s)$ and $Q_i(s)$ are then passed through low-pass filters for obtaining their average values P_{avgi} and Q_{avgi}, represented as [25]:

$$P_{avgi} = \frac{\omega_f}{s + \omega_f} P_i(s) \quad (9)$$

$$Q_{avgi} = \frac{\omega_f}{s + \omega_f} Q_i(s) \quad (10)$$

where ω_f is cut-off frequency of the low-pass filter. Its value is usually set low so that the inner voltage and current regulation loops are much faster than the outer droop power loop. Dynamics of the inner loops can thus be neglected [26], [27].

By next perturbing (2), (6), (9) and (10), the following perturbed expressions can be obtained, where Δ in front of a variable represents its small perturbed value around a defined equilibrium point.

$$\Delta \omega_i = -\frac{k_p \omega_f}{s + \omega_f} \Delta P_i + k_f \Delta V_{DCi} \quad (11)$$

$$\Delta V_i = -\frac{k_q \omega_f}{s + \omega_f} \Delta Q_i \quad (12)$$

Rewriting (11) and (12) in the time-domain results in the following expressions, where a dot above any variable represents derivative of that variable in time.

$$\Delta \dot{\omega}_i = -\omega_f \Delta \omega_i - k_p \omega_f \Delta P_i + k_f \Delta \dot{V}_{DCi} + k_f \omega_f \Delta V_{DCi} \quad (13)$$

$$\Delta \dot{V}_i = -\omega_f \Delta V_i - k_q \omega_f \Delta Q_i \quad (14)$$

Further noting that variation of energy E_i in the dc-link capacitor is related to its voltage V_{DCi}, (15) can be written, where C is the dc-link capacitance.

$$E_i = \int P_i(t)dt = \frac{1}{2}CV_{DCref}^2 - \frac{1}{2}CV_{DCi}^2 \quad (15)$$

The linear perturbed expression between the dc-link voltage and its power can thus be derived as follows, where m is the equilibrium point of V_{DCi}.

$$\Delta V_{DCi} = -\frac{1}{mCs} \cdot \Delta P_i = -\frac{k_{DC}}{s} \cdot \Delta P_i \quad (16)$$

Substituting $s\Delta V_{DCi} (= \Delta \dot{V}_{DCi})$ from (16) into (13) then results in:

$$\Delta \dot{\omega}_i = -\omega_f \Delta \omega_i - \left(k_p \omega_f + k_f k_{DC} \right) \Delta P_i + k_f \omega_f \Delta V_{DCi} \quad (17)$$

In addition, in the d-q reference frame, the vectorial form of the converter output voltage can be expressed as follows, where

$V_{di} = V_i\cos(\delta)$, $V_{qi} = V_i\sin(\delta)$ and $\delta_i = \arctan(V_{qi}/V_{di})$.

$$\overline{V}_i = V_{di} + jV_{qi} \tag{18}$$

From (18), a perturbed expression for $\Delta\delta_i$ can subsequently be derived as (19), where $m_{di} = -V_{qi}\big/\left(V_{di}^2 + V_{qi}^2\right)$ and $m_{qi} = V_{di}\big/\left(V_{di}^2 + V_{qi}^2\right)$.

$$\Delta\delta_i = m_{di}\Delta V_{di} + m_{qi}\Delta V_{qi} \tag{19}$$

Since $\Delta\omega_i = s\Delta\delta_i$, time-domain form of (19) changes to the following.

$$\Delta\omega_i = m_{di}\Delta \dot{V}_{di} + m_{qi}\Delta \dot{V}_{qi} \tag{20}$$

Noting next that the output voltage amplitude of (18) can be written as (21), from which its linearized perturbed expressions can be derived as (22) and (23) with $n_{di} = V_{di}\big/\sqrt{V_{di}^2 + V_{qi}^2}$ and $n_{qi} = V_{qi}\big/\sqrt{V_{di}^2 + V_{qi}^2}$.

$$V_i = \left|V_{di} + jV_{qi}\right| = \sqrt{V_{di}^2 + V_{qi}^2} \tag{21}$$

$$\Delta V_i = n_{di}\Delta V_{di} + n_{qi}\Delta V_{qi} \tag{22}$$

$$\Delta \dot{V}_i = n_{di}\Delta \dot{V}_{di} + n_{qi}\Delta \dot{V}_{qi} \tag{23}$$

From (14), (16), (17), (20) and (23), state equation for representing a single converter in Fig. 1(a) can eventually be derived as (24).

$$\begin{bmatrix} \Delta \dot{V}_{DCi} \\ \Delta \dot{\omega}_i \\ \Delta \dot{V}_{di} \\ \Delta \dot{V}_{qi} \end{bmatrix} = A_i \begin{bmatrix} \Delta V_{DCi} \\ \Delta \omega_i \\ \Delta V_{di} \\ \Delta V_{qi} \end{bmatrix} + B_i \begin{bmatrix} \Delta P_i \\ \Delta Q_i \end{bmatrix} \tag{24}$$

where

$$A_i = \begin{bmatrix} 0 & 0 & 0 & 0 \\ k_f\omega_f & -\omega_f & 0 & 0 \\ 0 & \dfrac{n_{qi}}{m_{di}n_{qi} - m_{qi}n_{di}} & \dfrac{m_{qi}n_{di}\omega_f}{m_{di}n_{qi} - m_{qi}n_{di}} & \dfrac{m_{qi}n_{qi}\omega_f}{m_{di}n_{qi} - m_{qi}n_{di}} \\ 0 & \dfrac{n_{di}}{m_{qi}n_{di} - m_{di}n_{qi}} & \dfrac{m_{di}n_{di}\omega_f}{m_{qi}n_{di} - m_{di}n_{qi}} & \dfrac{m_{di}n_{qi}\omega_f}{m_{qi}n_{di} - m_{di}n_{qi}} \end{bmatrix}$$

and

$$B_i = \begin{bmatrix} -k_{DC} & 0 \\ -k_p\omega_f - k_f k_{DC} & 0 \\ 0 & \dfrac{m_{qi}k_q\omega_f}{m_{di}n_{qi} - m_{qi}n_{di}} \\ 0 & \dfrac{m_{di}k_q\omega_f}{m_{qi}n_{di} - m_{di}n_{qi}} \end{bmatrix}.$$

B. Combined Model of Both Converters in Fig. 1(a)

The system in Fig. 1(a) with two two-stage RES converters can now be analyzed by first writing down the two converter voltages as $\dot{V}_1 = V_{d1} + jV_{q1}$ and $\dot{V}_2 = V_{d2} + jV_{q2}$, respectively. To avoid excessive complexity, line impedances of the two converters are also assumed equal, which together with the load impedance, are expressed as $r + jX$ and $R_L + jX_L$, respectively.

Applying Kirchhoff's Current Law then results in those output current expressions of the converters given in (25), which upon rearranged, leads to (26).

$$\begin{cases} \dot{I}_1 = \dfrac{\dot{V}_1\left[(r + R_L) + j(X + X_L)\right] - \dot{V}_2(R_L + jX_L)}{(r + jX)^2 + 2(R_L + jX_L)(r + jX)} \\[4mm] \dot{I}_2 = \dfrac{\dot{V}_2\left[(r + R_L) + j(X + X_L)\right] - \dot{V}_1(R_L + jX_L)}{(r + jX)^2 + 2(R_L + jX_L)(r + jX)} \end{cases} \tag{25}$$

$$\begin{cases} \dot{I}_1 = I_{d1} + jI_{q1} = Y_{11}V_{d1} + Y_{12}V_{q1} + Y_{13}V_{d2} + Y_{14}V_{q2} \\ \qquad + j\left(Y_{21}V_{d1} + Y_{22}V_{q2} + Y_{23}V_{d2} + Y_{24}V_{q2}\right) \\ \dot{I}_2 = I_{d2} + jI_{q2} = Y_{13}V_{d1} + Y_{14}V_{q1} + Y_{11}V_{d2} + Y_{12}V_{q2} \\ \qquad + j\left(Y_{23}V_{d1} + Y_{24}V_{q2} + Y_{21}V_{d2} + Y_{22}V_{q2}\right) \end{cases} \tag{26}$$

where

$$Y_{11} = \left(r^3 + 3R_L r^2 + X^2 r + 2X_L^2 r + 2R_L^2 r + 2X_L Xr + X^2 R_L\right)\big/Y_D,$$

$$Y_{12} = \Big(Xr^2 + X_L r^2 + 2R_L Xr + 2R_L^2 X \\ \qquad + 3X_L X^2 + 2X_L^2 X + X^3\Big)\Big/Y_D,$$

$$Y_{13} = \left(-R_L r^2 - 2X_L^2 r - 2X_L Xr - 2R_L^2 r + R_L X^2\right)\big/Y_D,$$

$$Y_{14} = \left(X_L r^2 - 2R_L Xr - 2R_L^2 X - 2X_L^2 X - X_L X^2\right)\big/Y_D,$$

$$Y_{21} = \Big(-X_L r^2 - Xr^2 - 2R_L Xr - X^3 \\ \qquad - 3X_L X^2 - 2R_L^2 X - 2X_L^2 X\Big)\big/Y_D,$$

$$Y_{22} = \left(r^3 + 3R_L r^2 + X^2 r + 2X_L^2 r + 2R_L^2 r + 2X_L Xr + R_L X^2\right)\big/Y_D,$$

$$Y_{23} = \left(-X_L r^2 + 2R_L Xr + X_L X^2 + 2R_L^2 X + 2X_L^2 X\right)\big/Y_D,$$

$$Y_{24} = \left(-R_L r^2 - 2X_L Xr - 2X_L^2 r - 2R_L^2 r + R_L X^2\right)\big/Y_D,$$

$$Y_D = X^4 + 4X_L X^3 + \left(4R_L r + 4R_L^2 + 4X_L^2 + 2r^2\right)X^2 \\ \qquad + 4r^2 X_L X + 4R_L^2 r^2 + 4X_L^2 r^2 + r^4 + 4r^3 R_L.$$

For convenience, (26) can further be rearranged in matrix form like shown below.

$$\begin{bmatrix} I_{d1} \\ I_{q1} \\ I_{d2} \\ I_{q2} \end{bmatrix} = \begin{bmatrix} Y_{11} & Y_{12} & Y_{13} & Y_{14} \\ Y_{21} & Y_{22} & Y_{23} & Y_{24} \\ Y_{13} & Y_{14} & Y_{11} & Y_{12} \\ Y_{23} & Y_{24} & Y_{21} & Y_{22} \end{bmatrix} \begin{bmatrix} V_{d1} \\ V_{q1} \\ V_{d2} \\ V_{q2} \end{bmatrix} \text{ or } [I] = [Y][V] \tag{27}$$

Perturbation and linearization of (27) then lead to:

$$[\Delta I] = [Y][\Delta V]. \tag{28}$$

Next, active and reactive powers of each converter can be computed using (29), which upon perturbed, leads to (30) and its simplified form in (31).

$$\begin{cases} P_i = V_{di}I_{di} + V_{qi}I_{qi} \\ Q_i = V_{qi}I_{di} - V_{di}I_{qi} \end{cases} \tag{29}$$

$$\begin{bmatrix} \Delta P_1 \\ \Delta Q_1 \\ \Delta P_2 \\ \Delta Q_2 \end{bmatrix} = \begin{bmatrix} I_{d1} & I_{q1} & 0 & 0 \\ -I_{q1} & I_{d1} & 0 & 0 \\ 0 & 0 & I_{d2} & I_{q2} \\ 0 & 0 & -I_{q2} & I_{d2} \end{bmatrix} \begin{bmatrix} \Delta V_{d1} \\ \Delta V_{q1} \\ \Delta V_{d2} \\ \Delta V_{q2} \end{bmatrix}$$

$$+ \begin{bmatrix} V_{d1} & V_{q1} & 0 & 0 \\ V_{q1} & -V_{d1} & 0 & 0 \\ 0 & 0 & V_{d2} & V_{q2} \\ 0 & 0 & V_{q2} & -V_{d2} \end{bmatrix} \begin{bmatrix} \Delta I_{d1} \\ \Delta I_{q1} \\ \Delta I_{d2} \\ \Delta I_{q2} \end{bmatrix} \tag{30}$$

$$[\Delta S] = [I][\Delta V] + [V][\Delta I] \tag{31}$$

Together, (28) and (31) give rise to:

$$[\Delta S] = ([I] + [V][Y])[\Delta V] \tag{32}$$

which when considered with (24), leads to the following expression.

$$\left[\Delta \dot{X}\right] = \begin{bmatrix} A_1 & 0 \\ 0 & A_2 \end{bmatrix}[\Delta X] + \begin{bmatrix} B_1 & 0 \\ 0 & B_2 \end{bmatrix}\left([I]+[V][Y]\right)\begin{bmatrix} \Delta V_{d1} \\ \Delta V_{q1} \\ \Delta V_{d2} \\ \Delta V_{q2} \end{bmatrix} \tag{33}$$

where

$$[\Delta X] = \begin{bmatrix} \Delta V_{DC1} & \Delta\omega_1 & \Delta V_{d1} & \Delta V_{q1} & \Delta V_{DC2} & \Delta\omega_2 & \Delta V_{d2} & \Delta V_{q2} \end{bmatrix}^{\mathrm{T}}.$$

$$\begin{bmatrix} \Delta V_{d1} \\ \Delta V_{q1} \\ \Delta V_{d2} \\ \Delta V_{q2} \end{bmatrix} = \begin{bmatrix} 0 & 0 & 1 & 0 & 0 & 0 & 0 & 0 \\ 0 & 0 & 0 & 1 & 0 & 0 & 0 & 0 \\ 0 & 0 & 0 & 0 & 0 & 0 & 1 & 0 \\ 0 & 0 & 0 & 0 & 0 & 0 & 0 & 1 \end{bmatrix}\begin{bmatrix} \Delta V_{DC1} \\ \Delta\omega_1 \\ \Delta V_{d1} \\ \Delta V_{q1} \\ \Delta V_{DC2} \\ \Delta\omega_2 \\ \Delta V_{d2} \\ \Delta V_{q2} \end{bmatrix} = [k]\begin{bmatrix} \Delta V_{DC1} \\ \Delta\omega_1 \\ \Delta V_{d1} \\ \Delta V_{q1} \\ \Delta V_{DC2} \\ \Delta\omega_2 \\ \Delta V_{d2} \\ \Delta V_{q2} \end{bmatrix} \tag{34}$$

Substituting (34) to (33) then leads to:

$$\left[\Delta \dot{X}\right] = \left\{ \begin{bmatrix} A_1 & 0 \\ 0 & A_2 \end{bmatrix} + \begin{bmatrix} B_1 & 0 \\ 0 & B_2 \end{bmatrix}\left([I]+[V][Y]\right)[k] \right\}[\Delta X]. \tag{35}$$

The state space matrix M for the two converters in Fig. 1(a) can eventually be expressed as:

$$M = \begin{bmatrix} A_1 & 0 \\ 0 & A_2 \end{bmatrix} + \begin{bmatrix} B_1 & 0 \\ 0 & B_2 \end{bmatrix}\left([I]+[V][Y]\right)[k]. \tag{36}$$

C. Eigenvalue Analysis

System response of the example network in Fig. 1(a) can be analyzed by plotting its root loci using (35) and parameters $\dot{V}_1 = \dot{V}_2 = 218 + j30$ V for the converters, $Z_L = 50 + j0.2\,\Omega$ for the load, $Z = 0.2 + j1.8\,\Omega$ for the distribution lines, and $\omega_f = 3.141$ for the filter cut-off frequency used for computing the average powers. Fig. 5 shows the obtained root loci with droop parameters $k_p = 0.0003$, $k_f = 0.001$ and k_q varying from 0.0001 to 0.01. The immediate observation seen from the figure is an eigenvalue at the origin, which to some extent, is expected since the system matrix is singular. Moreover, only two poles λ_1 and λ_2 are found to affect the system dynamics since the other poles are far away from the imaginary axis. Regardless of that, the overall system is stable since all poles are in the left-half s-plane.

Complementing, Fig. 6 shows another set of root loci obtained with $k_q = 0.008$, $k_f = 0.001$ and k_p varying from 0.00001 to 0.001. The varying parameter is now k_p and not k_q, which when increased, will cause λ_6 to move closer to the origin and hence raising its effect. The dominant poles λ_1 and λ_2 will
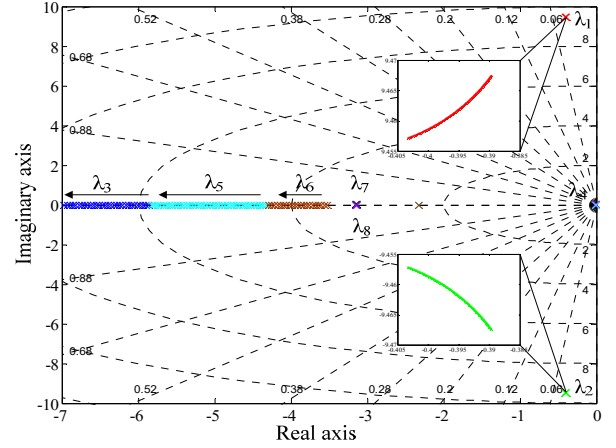

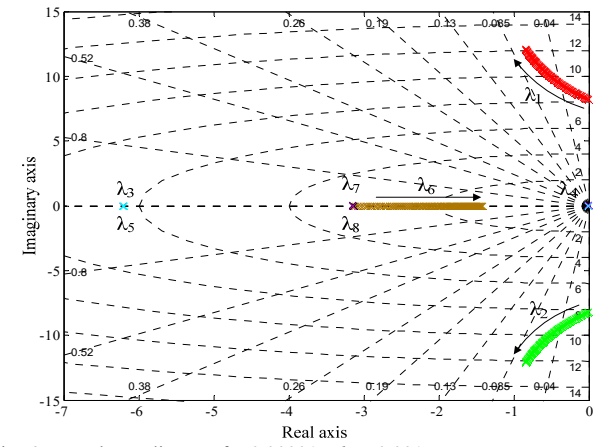Fig. 5. Root locus diagram for $0.0001 \le k_q \le 0.01$.

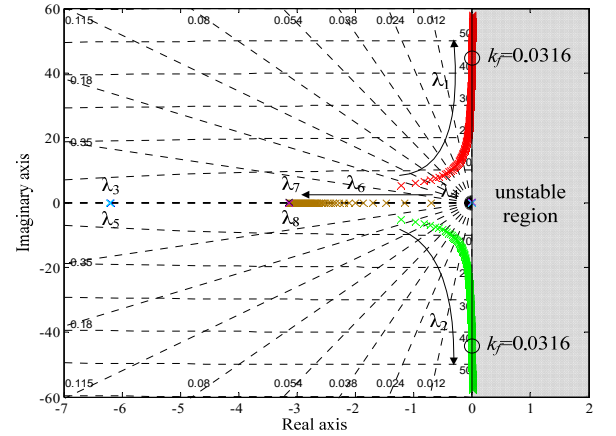Fig. 6. Root locus diagram for $0.00001 \le k_p \le 0.001$.

Fig. 7. Root locus diagram for $0.0001 \le k_f \le 0.05$.

however shift away from the imaginary axis as k_p increases. Their combined effect is thus an improvement of the system dynamics. Increasing k_p will however cause large frequency drop in the steady state according to the traditional droop expressions given in (1). Selection of k_p should therefore be based on an acceptable trade-off between dynamics and steady-state drop.

Referring next to Fig. 7, a third set of root loci is plotted with $k_p = 0.0003$, $k_q = 0.008$ and k_f varying from 0.0001 to 0.05. The
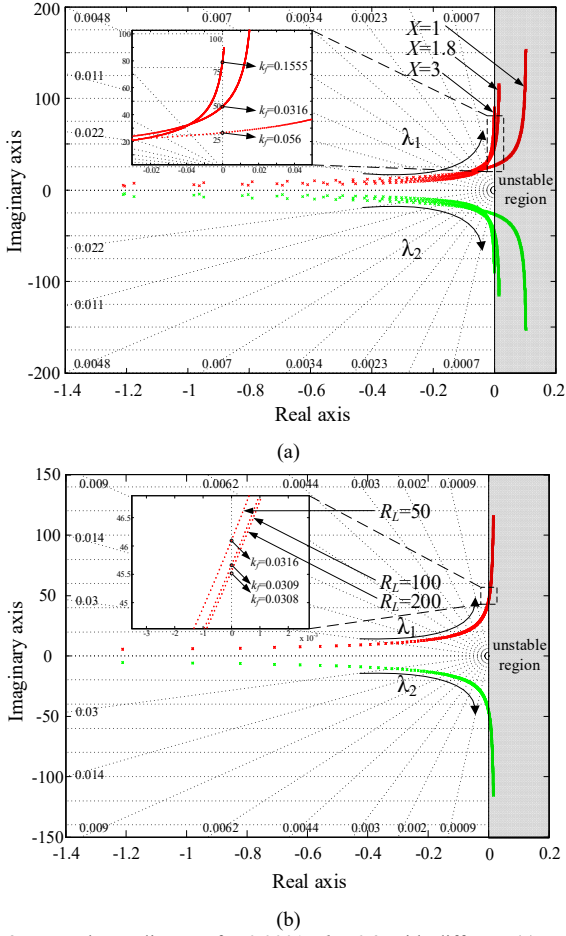
Fig. 8. Root locus diagram for $0.0001 \leq k_f \leq 0.2$ with different (a) reactive values for inductive distribution lines and (b) resistive values for load.

increased parameter is now k_f, which will cause dominant poles λ_1 and λ_2 to shift closer to the imaginary axis. The system response is therefore more oscillatory, and will eventually become unstable as k_f rises above 0.0316 (λ_1 and λ_2 enter the right-half s-plane). This instability crossing point of k_f will, in fact, change with line and load impedances, as demonstrated in Fig. 8. More specifically, the root loci in Fig. 8(a) shows that as reactive component X of predominantly inductive lines increases, instability is entered only after k_f crosses a higher critical value (0.056, 0.0316 and then 0.1555 in Fig. 8(a)). Similarly, by decreasing resistive component R_L of the load, a slightly wider stable range for k_f is observed in Fig. 8(b) (crossing point moves from 0.0308 to 0.0309, and then to 0.0316). The final k_f chosen must hence meet the "worst case" requirements at low X and high R_L.

VI. SIMULATION RESULTS

As a simple preliminary verification, two similarly rated RESs have been simulated using Matlab/Simulink. Parameters used for the RESs are given in Table I, similar to those used for the subsequent experimental testing. Results obtained with the proposed dual droop scheme are shown in Fig. 9(a) and (b) for predominantly inductive and resistive lines, respectively. Referring to Fig. 9(a) as an example, before 0.2s, the two RESs are assumed to harness a maximum of 550W each. They should
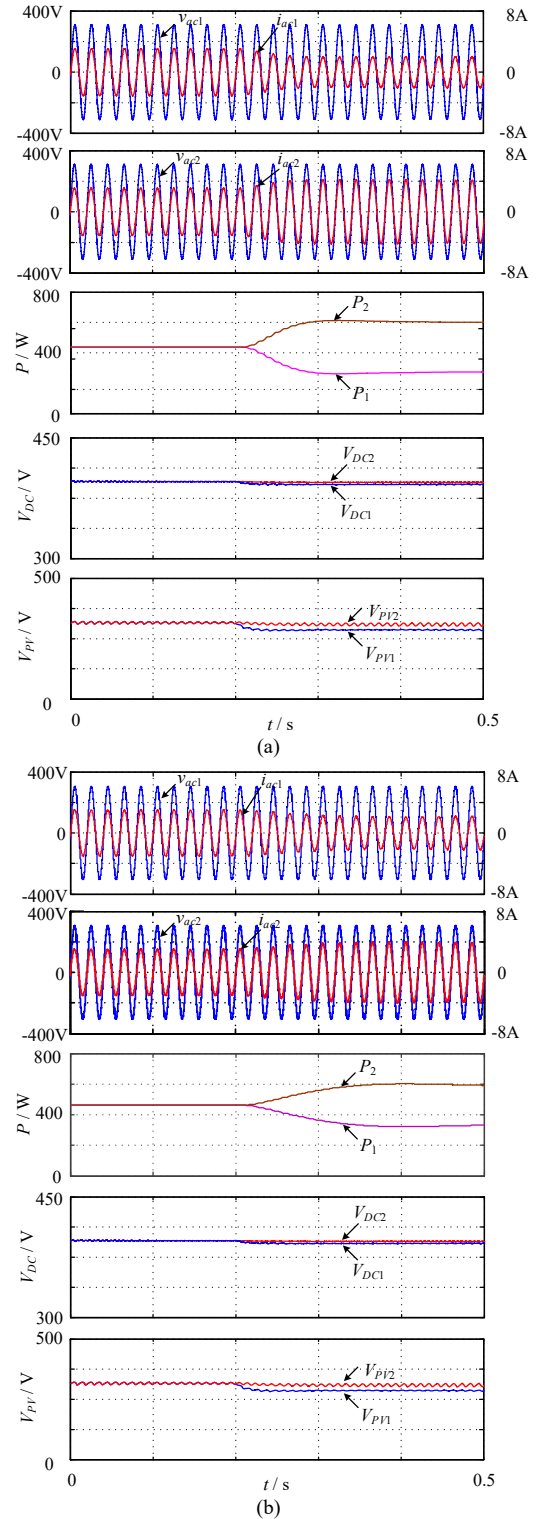
Fig. 9. Simulated results using dual droop scheme. (a) Inductive lines with $k_f = 0.01$, and (b) resistive lines with $k_V = 1$.

hence share the active load demand evenly with their respective dc-link voltages kept at 400V. These expectations have respectively been verified by the third and fourth plots of Fig. 9(a) before 0.2s.

After 0.2s, the maximum capacity of RES1 has been lowered from 550W to 310W, while that of RES2 has been kept

TABLE I
PARAMETERS USED FOR TESTED SYSTEM

Parameter		Values
PV panel voltage variation (V_{PV})		200V-350V
Rated output voltage amplitude of PV inverter (V_{0n})		220V(rms)
Rated frequency of PV inverter (f_{0n})		50Hz
DC-link reference voltage (V_{DCref})		400V
DC-link capacitance (C)		940μF
Boost inductance (L)		4mH
Output filter inductance (L_{ac})		6mH
Output filter capacitance (C_{ac})		10μF
Common boost and inverter switching frequency (f_s)		10kHz
Load (Z_{load})		44Ω
Inductive	Active droop coefficient (k_{pi})	0.0003rad/(s•W)
	Reactive droop coefficient (k_{qi})	0.008V/Var
	Impedance of transmission line ($Z_{inductive}$)	0.1Ω, 3mH
Resistive	Active droop coefficient (k_{pi})	0.004V/(s•W)
	Reactive droop coefficient (k_{qi})	0.001rad/Var
	Impedance of transmission line ($Z_{resistive}$)	2Ω, 0.8μH
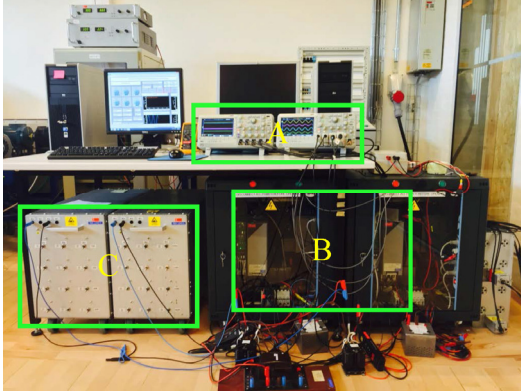
Fig. 10. Laboratory setup: A - oscilloscope, B - converters, and C - load.

unchanged. RES1, being unable to provide sufficient active power, will then experience dc-link voltage drop like in the fourth plot of Fig. 9(a). The amount of drop depends on the size of dc-link capacitance used, but regardless of that, it will cause the droop line of RES1 to shift down like in Fig. 2, until the droop-demanded active power reaches 310W like in the third plot of Fig. 9(a). Simultaneously, RES2 supplies more active power to the load in order to cover shortfall caused by RES1. This increase from RES2 can also be seen from the third plot of Fig. 9(a). Additionally, the last plot of Fig. 9(a) shows both PV input voltages dropping from 315V to 275V for RES1 and 315V to 305V for RES2. As explained earlier with Fig. 2, the larger drop of RES1 is caused by jumping from "a" to "b_1" on different PV curves, while the smaller drop of RES2 is caused by shifting from "a" to "b_2" along the same PV curve. The proposed dual droop scheme has therefore responded, as intended.

VII. EXPERIMENTAL RESULTS

To verify the proposed dual droop scheme, experiments have been performed with the example network shown in Fig. 1(a). Hardware setup for the experiments is shown in Fig. 10, while its parameters are given in Table I. Included in the setup is a dSPACE DS1103 controller for implementing the dual droop
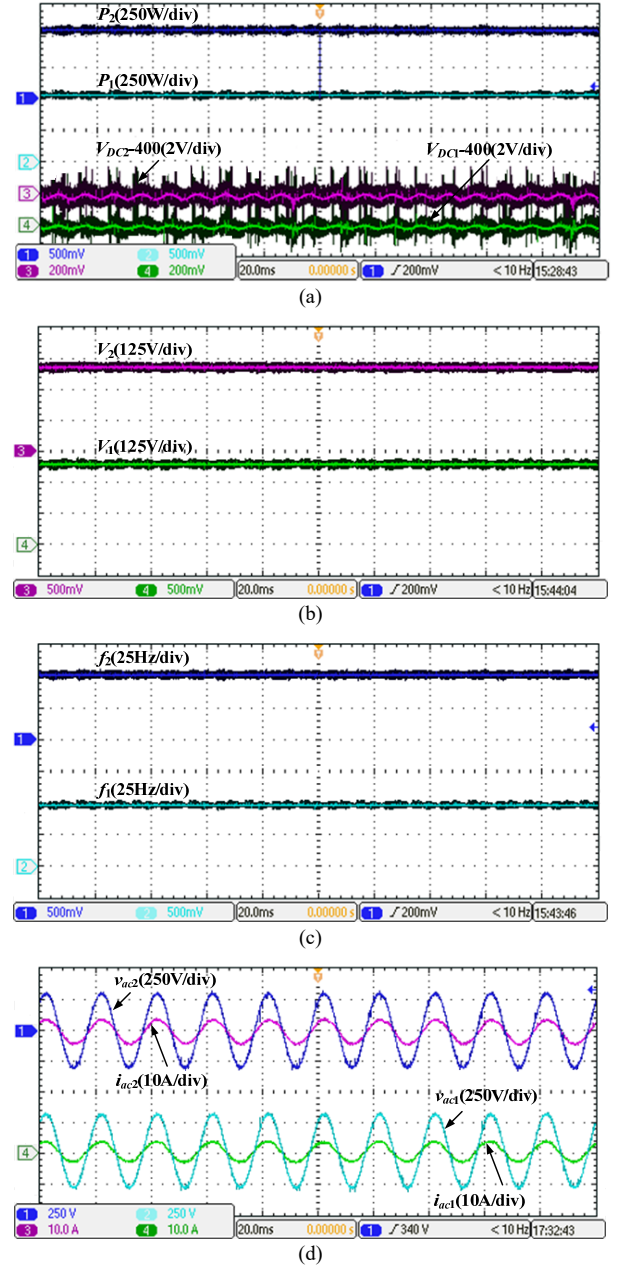

(a)

(b)

(c)

(d)

Fig. 11. Experimental results using inductive dual droop scheme with k_f = 0.01. (a) Output active powers P_1, P_2 and dc-link voltages V_{DC1}-400, V_{DC2}-400, (b) output voltage amplitudes V_1, V_2, (c) output voltage frequencies f_1, f_2, and (d) output voltage v_{ac1}, v_{ac2} and output current i_{ac1}, i_{ac2}.

scheme, which when enabled, gives rise to those results described below.

A. Inductive Lines

Fig. 11 shows experimental results captured with the dual droop scheme and k_f = 0.01 when the output active power capacities of the two RESs are at their common rated value of 800W, and hence sufficient for powering the total load of 1.1kW. The proposed droop scheme will thus ensure that they share the load evenly like when using the traditional droop scheme. Waveforms associated with the two RESs are thus similar with even power sharing of $P_1 = P_2 = 550$W confirmed
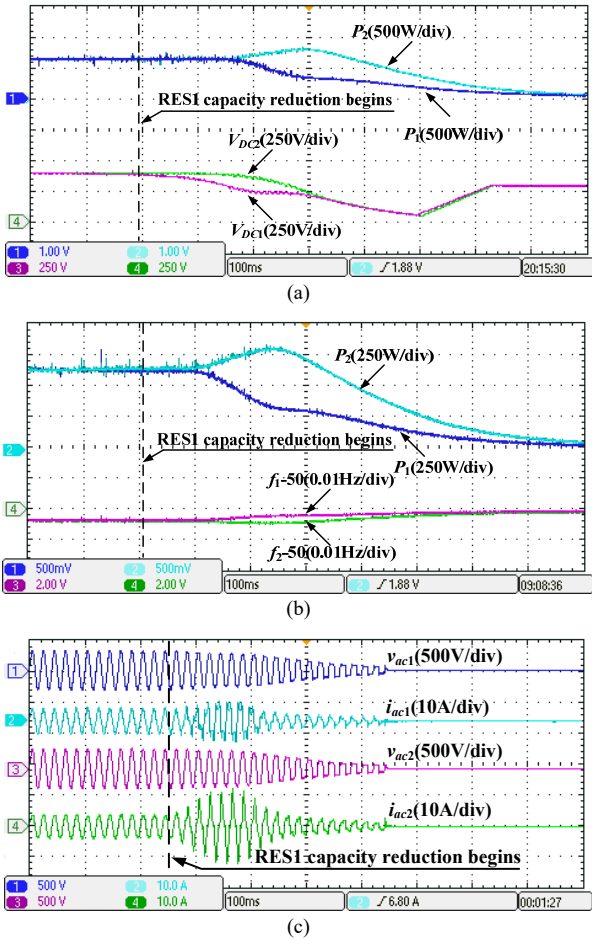
Fig. 12. Experimental results using inductive traditional droop scheme with RES1 capacity reduction. (a) Output active powers P_1, P_2 and dc-link voltages V_{DC1}, V_{DC2}, (b) output active powers P_1, P_2 and output voltage frequencies f_1-50, f_2-50, and (c) output voltage v_{ac1}, v_{ac2} and output current i_{ac1}, i_{ac2}.
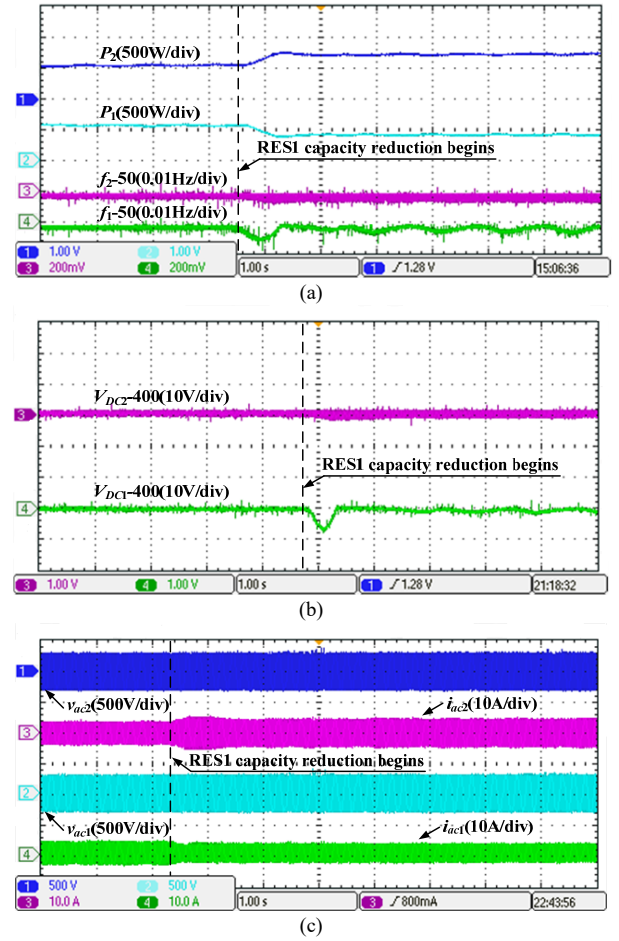
Fig. 13. Experimental results using inductive dual droop scheme with RES1 capacity reduction and $k_f = 0.01$. (a) Output active powers P_1, P_2 and output voltage frequencies f_1-50, f_2-50, (b) dc-link voltages V_{DC1}-400, V_{DC2}-400, and (c) output voltage v_{ac1}, v_{ac2} and output current i_{ac1}, i_{ac2}.

in Fig. 11(a).

Performances of the traditional and dual droop schemes will only differ when one RES has its capacity reduced significantly due to intermittency. To demonstrate the differences, Fig. 12 shows the experimental results produced by the traditional droop scheme when the source capacity of RES 1 reduces from 800W to 400W. RES1 is thus no longer able to provide the demanded droop power of 550W. In contrast, capacity of RES2 remains unchanged at 800W, and can hence shoulder more load. Droop schemes of both RESs are therefore in conflict with RES1 demanding for an increase in frequency to lower its droop power command and RES2 demanding for a decrease in frequency to raise its generation for filling the energy shortfall introduced by RES1.

The conflict can be seen in Fig. 12(b), where f_1 and f_2 deviate after triggering the transient. The shortage of energy in RES1 also causes its dc-link voltage V_{DC1} to drop more rapidly. This fall, together with the inability to arrive at a common steady-state frequency, eventually causes the RESs to trip. Powers P_1 and P_2, terminal voltages v_{ac1} and v_{ac2}, and output currents i_{ac1} and i_{ac2} of the RESs are therefore gradually reduced to zero, as seen from the three plots in Fig. 12.

The breakdown can however be avoided by the proposed dual droop scheme, as seen from Fig. 13 obtained with the same disturbance and $k_f = 0.01$. As anticipated, dc-link voltage V_{DC1} of RES1 drops, which in turn causes droop line of RES1 to be brought down by a non-zero $\Delta\omega_1$ (solid to dashed line in Fig. 2). Droop power command of RES1 can therefore be brought down by a decrease, rather than increase, in frequency. The decrease in frequency also permits generation of RES2 to increase to fill energy shortfall introduced by RES1. A common steady-state frequency and an eventually stabilized V_{DC1} can hence be reached, permitting the network to continue operation, as seen from all plots shown in Fig. 13.

To next demonstrate the effect of k_f, a smaller $k_f = 0.001$ is used to obtain Fig. 14, which in effect, is similar to Fig. 13. The only differences are a larger dip in V_{DC1} and a longer setting time observed in Fig. 14. Explanation for these can be deduced from Fig. 2 and Subsection IV(C). Firstly, Fig. 2 informs that the new operating points of Fig. 13 and 14 are at or close to the same peak point "b_1" of the lowered PV curve. They are therefore at the boundary of the positive-sloping side of the PV curve, which according to Subsection IV(C), requires the dual droop scheme for maintaining a stable operating point in the
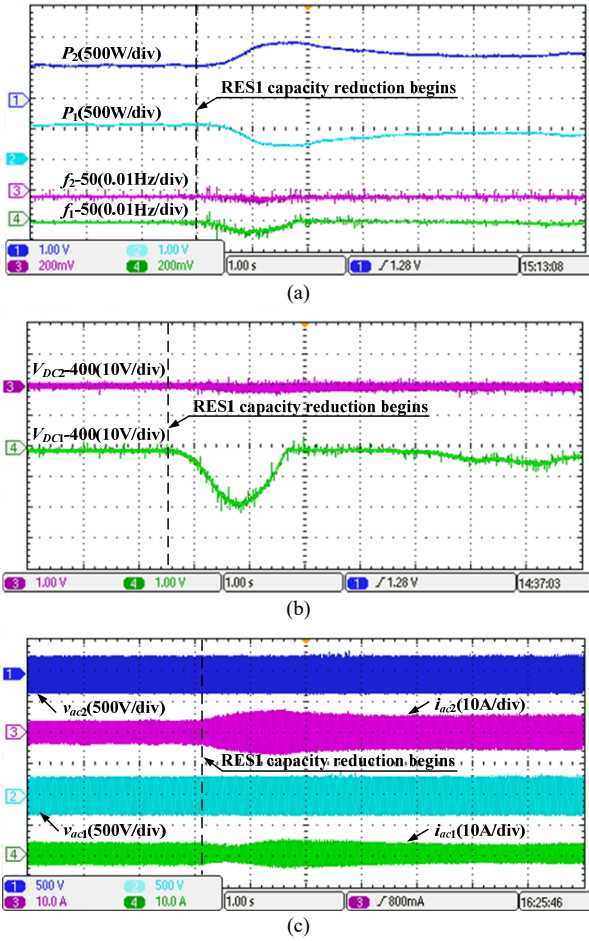
Fig. 14. Experimental results using inductive dual droop scheme with RES1 capacity reduction and k_f = 0.001. (a) Output active powers P_1, P_2 and output voltage frequencies f_1-50, f_2-50, (b) dc-link voltages V_{DC1}-400, V_{DC2}-400, and (c) output voltage v_{ac1}, v_{ac2} and output current i_{ac1}, i_{ac2}.

steady state. Droop gain k_f should therefore not be small, which when reduced to zero, represents the traditional droop scheme. This explains the more oscillatory V_{DC1} in Fig. 14 caused by its smaller k_f = 0.001. On the other hand, k_f should not be larger than the limit identified in Fig. 7, above which instability will surface even along the negative-sloping side of the PV curve.

B. Resistive Lines

The experiments have been repeated with predominantly resistive lines used for connecting the two two-stage RESs shown in Fig. 1(a). Fig. 15 shows the corresponding results obtained with the dual droop scheme and k_V = 1 when both sources are at their common rated capacity of 800W. They should therefore share the total load of 1.1kW evenly (not exactly equal since small mismatch in line resistances will always exist), and their dc-link voltages will be stable. These results will also be produced by the traditional droop scheme since the dual droop and traditional schemes differ only when one of the sources does not have enough capacity for satisfying its droop power command.

To illustrate, Fig. 16 shows results of the traditional droop scheme when the capacity of RES1 has been lowered from 550W to 380W, and hence not able to supply the droop power
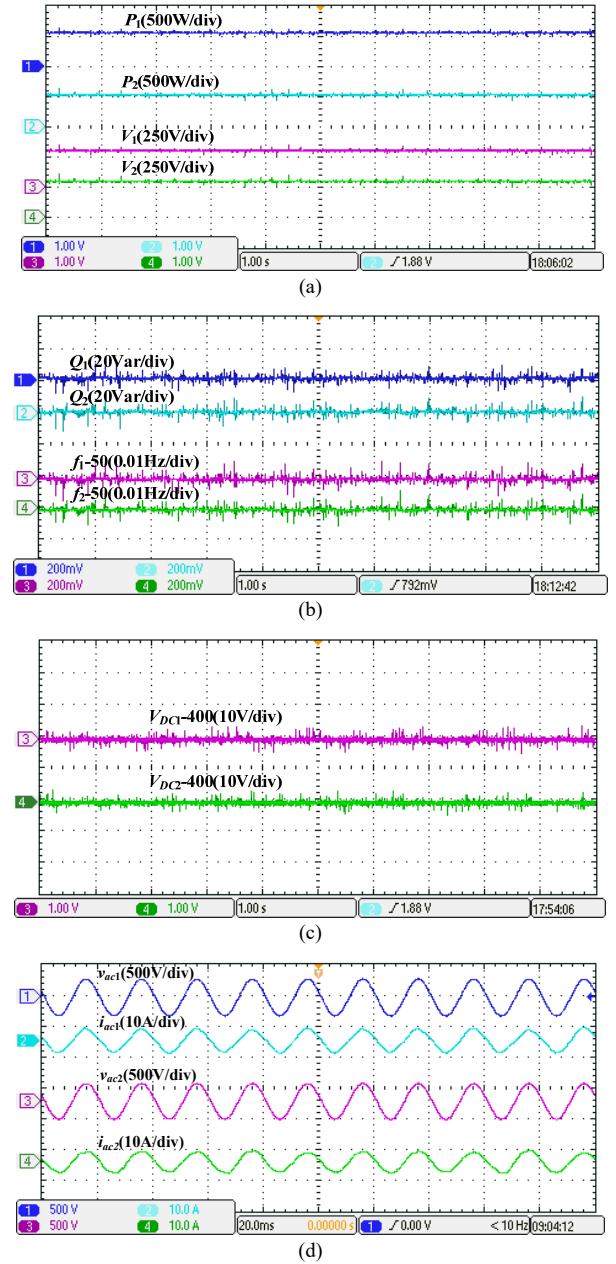

Fig. 15. Experimental results using resistive dual droop scheme with k_V = 1. (a) Output active powers P_1, P_2 and output voltage amplitudes V_1, V_2, (b) output reactive powers Q_1, Q_2 and output voltage frequencies f_1-50, f_2-50, (c) dc-link voltages V_{DC1}-400, V_{DC2}-400, and (d) output voltage v_{ac1}, v_{ac2} and output current i_{ac1}, i_{ac2}.

command. Anticipated responses are thus a deviation of the two converter terminal voltages and a sizable drop of dc-link voltage V_{DC1} of RES1. Both RESs are eventually tripped with their powers, terminal voltages and output currents gradually brought to zero, as observed in Fig. 16.

To avoid the breakdown, the dual droop scheme is used to obtain those results shown in Fig. 17 and Fig. 18 when subject to the same disturbance, but with a larger k_V = 1 used for the former and a smaller k_V = 0.5 used for the latter. The larger k_V causes dc-link voltage V_{DC1} to drop lesser in Fig. 17(a), as compared to Fig. 18(a). Regardless of that, waveforms in both figures can reach their respective new steady states, which
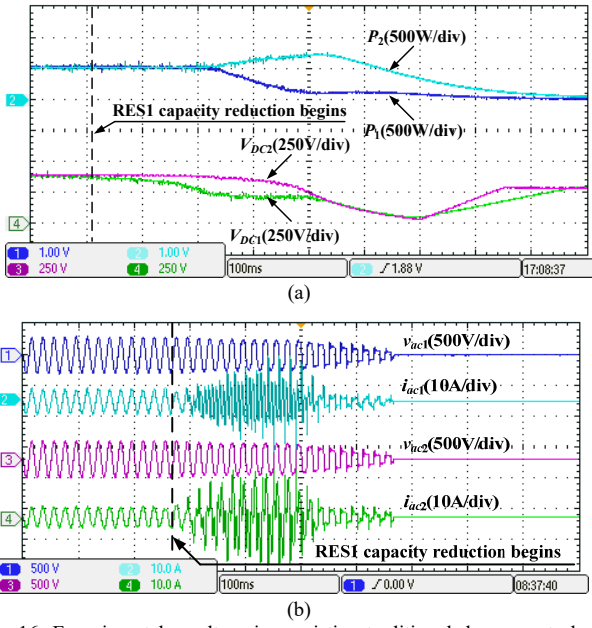
Fig. 16. Experimental results using resistive traditional droop control with RES1 capacity reduction. (a) Output active powers P_1, P_2 and dc-link voltages V_{DC1}, V_{DC2}, and (b) output voltage v_{ac1}, v_{ac2} and output current i_{ac1}, i_{ac2}.
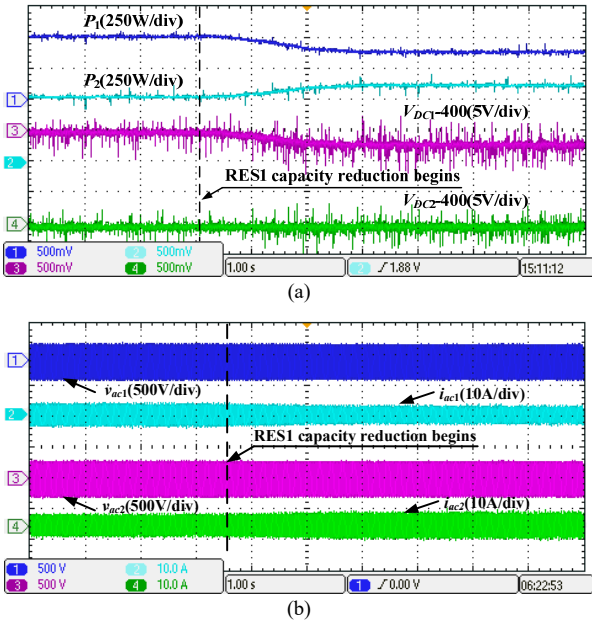

Fig. 17. Experimental results using resistive dual droop scheme with RES1 capacity reduction and $k_V = 1$. (a) Output active powers P_1, P_2 and dc-link voltages V_{DC1}-400, V_{DC2}-400, and (b) output voltage v_{ac1}, v_{ac2} and output current i_{ac1}, i_{ac2}.

certainly, is the intended outcome of the proposed dual droop scheme for controlling two-stage RES converters.

VIII. CONCLUSION

Conventional droop schemes for converters have mostly assumed that active droop power commands can be met by sources connected to the converters. This may not be true with RESs because of intermittency. An improved dual droop
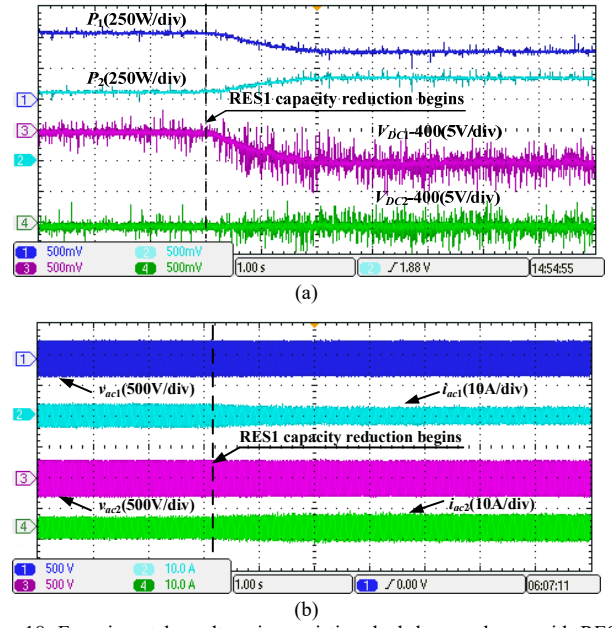

Fig. 18. Experimental results using resistive dual droop scheme with RES1 capacity reduction and $k_V = 0.5$. (a) Output active powers P_1, P_2 and dc-link voltages V_{DC1}-400, V_{DC2}-400, and (b) output voltage v_{ac1}, v_{ac2} and output current i_{ac1}, i_{ac2}.

scheme has thus been proposed for controlling two-stage converters powered by RESs. The thought is to re-apply the droop principle to the dc-link voltage of each converter, which instead of being held constant, is permitted to drop by a small amount whenever its RES capacity cannot met its droop power command. The drop in dc-link voltage can then be used for lowering the droop line of the converter so that its droop power command can be reduced by decreasing, rather than increasing, frequency or voltage depending on whether the lines are predominantly inductive or resistive. The lowered frequency or voltage in turn allows the other converter with enough source capacity to raise its generation for replenishing any energy shortfall. The overall system is thus stable with resilient active power sharing, as proven through root locus analysis and experimental testing.

REFERENCES

[1] C. T. Lee, C. C. Chu, and P. T. Cheng, "A new droop control method for the autonomous operation of distributed energy resource interface converters," IEEE Trans. Power Electron., vol. 28, no. 4, pp. 1980–1993, Apr. 2013.

[2] M. Amirabadi, A. Balakrishnan, H. A. Toliyat, and W. C. Alexander, "High-frequency ac-link PV inverter," *IEEE Trans. Ind. Electron.*, vol. 61, no. 1, pp. 281–291, Jan. 2014.

[3] H. Mahmood, D. Michaelson, and J. Jiang, "Accurate reactive power sharing in an islanded microgrid using adaptive virtual impedances," *IEEE Trans. Power Electron.*, vol. 30, no. 3, pp. 1605–1617, Mar. 2015.

[4] Y. Tao, Q. W. Liu, Y. Deng, X. H. Liu, and X. N. He, "Analysis and mitigation of inverter output impedance impacts for distributed energy resource interface," *IEEE Trans. Power Electron.*, vol. 30, no. 7, pp. 3563–3576, Jul. 2015.

[5] T. K. S. Freddy, N. A. Rahim, W. P. Hew, and H. S. Che, "Comparison and analysis of single-phase transformerless grid-connected PV inverters," *IEEE Trans. Power Electron.*, vol. 29, no. 10, pp. 5358–5369, Oct. 2014.

[6] R. G. Wandhare, and V. Agarwal, "Novel integration of a PV-wind energy system with enhanced efficiency," *IEEE Trans. Power Electron.*, vol. 30, no. 7, pp. 3638–3649, Jul. 2015.

[7] U. M. Choi, F. Blaabjerg, and K. B. Lee, "Control strategy of two capacitor voltages for separate MPPTs in photovoltaic systems," *IEEE Trans. Power Electron.*, vol. 51, no. 4, pp. 3295–3303, Jul./Aug. 2015.

[8] Y. Hu, J. Zhang, W. Cao, J. Wu, G. Y. Tian, S. J. Finney, and J. L. Kirtley, "Online two-section PV array fault diagnosis with optimized voltage sensor locations," *IEEE Trans. Ind. Electron.*, vol. 62, no. 11, pp. 7237–7246, Nov. 2015.

[9] A. Kahrobaeian and Y. A. -R. I. Mohamed, "Analysis and mitigation of low-frequency instabilities in autonomous medium-voltage converter-based microgrids with dynamic loads," *IEEE Trans. Ind. Electron.*, vol. 61, no. 4, pp. 1643–1658, Apr. 2014.

[10] P. Wang, C. Jin, D. X. Zhu, Y. Tang, P. C. Loh, and F. H. Choo, "Distributed control for autonomous operation of a three-port AC/DC/DS hybrid microgrid," *IEEE Trans. Ind. Electron.*, vol. 62, no. 2, pp. 1279–1290, Feb. 2015.

[11] H. Han, Y. Sun, M. Su, and J. M. Guerrero, "An improved droop control strategy for reactive power sharing in islanded microgrid," *IEEE Trans. Power Electron.*, vol. 30, no. 6, pp. 3133–3141, Jun. 2015.

[12] J. W. He, Y. W. Li, and F. Blaabjerg, , "An enhanced islanding microgeid reactive power, imbalance power, and harmonic power sharing scheme," *IEEE Trans. Power Electron.*, vol. 30, no. 6, pp. 3389–3401, Jun. 2015.

[13] M. E. -S. Ahmed, M. Orabi, and O. M. Abdelrahim, "Two-stage micro-grid inverter with high-voltage gain for photovoltaic applications," *IET Power Electron.*, vol. 6, no. 9, pp. 1812–1821, 2013.

[14] N. E. Zakzouk, A. K. Abdelsalam, A. A. Helal, and B. W. Williams, "DC-link voltage sensorless control technique for single-phase two-stage photovoltaic grid-connected system," in *Proc. ENERGYCON,* 2014, pp. 58–64.

[15] D. Debnath, and K. Chatterjee, "Two-stage solar Photovoltaic-based stand-alone scheme having battery as energy storage element for rural deloyment," *IEEE Trans. Ind. Electron.*, vol. 62, no. 7, pp. 4148–4157, Jul. 2015.

[16] D. Velaso DE La Fuente, C. L. T. Rodriguez, G. Garcero, E. Figueres, and R. O. Gonzalez, "Photovoltaic power system with battery backup with grid-connected and islanded operation capabilities," *IEEE Trans. Ind. Electron.*, vol. 60, no. 4, pp. 1571–1582, Apr. 2013.

[17] C. Trujillo Rodriguez, D. Velasco De La Fuente, G. Garcera, E. Figueres, and J. A. Guacaneme Moreno, "Reconfigurable control scheme for a PV microinverter working in both grid-connected and island modes," *IEEE Trans. Ind. Electron.*, vol. 60, no. 4, pp. 1582–1595, Apr. 2013.

[18] W. Du, Q. R. Jiang, M. J. Erickson, and R. H. Lasseter, "Voltage-source control of PV inverter in a CERTS microgrid," *IEEE Trans. Power Del.*, vol. 29, no. 4, pp. 1726–1734, Aug. 2014.

[19] A. Elrayyah, Y. Sozer, and M. E. Elbuluk, "Modeling and control design of microgrid-connected PV-based sources," *IEEE Trans. Power Electron.*, vol. 2, no. 4, pp. 907–919, Dec. 2014.

[20] A. Elrayyah, Y. Sozer, and M. Elbuluk, "Microgrid-connected PV-based sources: a novel autonomous control method for maintaining maximum power," *IEEE Ind. Applicat. Mag.*, vol. 21, no. 2, pp. 19–29, Mar./Apr. 2015.

[21] D. Wu, F. Tang, T. Dragicevic, J. C. Vasquez, and J. M. Guerrero, "A control architecture to coordinate renewable energy sources and energy storage systems in islanded microgrids," *IEEE Trans. Smart Grid.*, vol. 6, no. 3, pp. 1156–1166, May 2015.

[22] H. Mahmood, D. Michaelson, and J. Jiang, "Strategies for independent deployment and autonomous control of PV and battery units in islanded microgrids," *IEEE J. Emerg. Sel. Topics Power Electron.*, vol. 3, no. 3, pp. 742–755, Sep. 2015.

[23] S. V. Iyer, M. N. Belur, and M. C. Chandorka, "A generalized computational method to determine stability of a multi-inverter microgrid," *IEEE Trans. Power Electron.*, vol. 25, no. 9, pp. 2420–2432, Sep. 2010.

[24] W. R. Issa, M. A. Abusara, and S. M. Sharkh, "Control of transient power during unintentional islanding of microgrids," *IEEE Trans. Power Electron.*, vol. 30, no. 8, pp. 4573–4584, Aug. 2015.

[25] E. A. A. Coelho, P. C. Cortizo, and P. F. D. Garcia, "Small-signal stability for parallel-connected inverters in stand-alone AC supply systems," *IEEE Trans. Ind. Applicat.*, vol. 38, no. 2, pp. 533–542, Mar./Apr. 2002.

[26] X. Q. Guo, Z. G. Lu, B. C. Wang, X. F. Sun, L. Wang, and J. M. Guerrero, "Dynamic phasors-based modeling and stability analysis of droop-controlled inverters for microgrid applications," *IEEE Trans. Smart Grid,* vol. 5, no. 6, pp. 2980–2987, Nov. 2014.

[27] T. L. Vandoorn, B. Meersman, J. D. M. De Kooning, and L. Vandevelde, "Analogy between conventional grid control and island microgrid control based on a global DC-link voltage droop," *IEEE Trans. Power Delt.*, vol. 27, no. 3, pp. 1405–1414, Jul. 2012.

Hongpeng Liu (M'13) received his B.S. degree in Electrical Engineering from Harbin University of Science and Technology, Harbin, China, in 2000, and his M.S. and Ph.D. degrees in Electrical Engineering from Harbin Institute of Technology, Harbin, China, in 2006 and 2011, respectively. In 2011, he joined Harbin Institute of Technology as an Assistant Professor in the Department of Electrical Engineering. His current research interests include photovoltaic generation, Micro-grid, and PWM converter/inverter systems.

Yongheng Yang (S'12–M'15) received the B.Eng. degree in 2009 from Northwestern Polytechnical University, China and the Ph.D. degree in 2014 from Aalborg University, Denmark.

He was a postgraduate with Southeast University, China, from 2009 to 2011. In 2013, he was a Visiting Scholar with Texas A&M University, USA. Since 2014, he has been with the Department of Energy Technology, Aalborg University, where currently he is an Assistant Professor. His research interests are focused on grid integration of renewable energy systems, power converter design, analysis and control, harmonics identification and mitigation, and reliability in power electronics. Dr. Yang has published more than 80 technical papers and co-authored a book – *Periodic Control of Power Electronic Converters* (London, UK: IET, 2017).

Dr. Yang is a Member of the IEEE Power Electronics Society (PELS) Students and Young Professionals Committee, where he serves as the Global Strategy Chair and responsible for the IEEE PELS Students and Young Professionals Activities. He served as a Guest Associate Editor of IEEE JOURNAL OF EMERGING AND SELECTED TOPICS IN POWER ELECTRONICS, and has also been invited as a Guest Editor of *Applied Sciences*. He is an active reviewer for relevant top-tier journals.
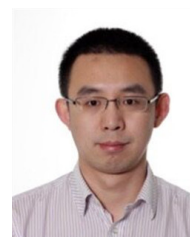
Xiongfei Wang (S'10–M'13) received the B.S. degree from Yanshan University, Qinhuangdao, China, in 2006, the M.S. degree from Harbin Institute of Technology, Harbin, China, in 2008, both in electrical engineering, and the Ph.D. degree from Aalborg University, Aalborg, Denmark, in 2013. Since 2009, he has been with the Aalborg University, Aalborg, Denmark, where he is currently an Assistant Professor in the Department of Energy Technology. His research interests include modeling and control of grid-connected converters, harmonics analysis and control, passive and active filters, stability of power electronic based power systems.

He received an IEEE Power Electronics Transactions Prize Paper award in 2014. He serves as the Associate Editor of IEEE Transactions on Industry Applications and the Guest Associate Editor of IEEE Journal of Emerging and Selected Topics in Power Electronics Special Issue on Distributed Generation.

Poh Chiang Loh received his B. Eng (Hons) and M.Eng from the National University of Singapore in 1998 and 2000 respectively, and his Ph.D from Monash University, Australia, in 2002, all in electrical engineering. His interests are in power converters and their grid applications.

Frede Blaabjerg (S'86–M'88–SM'97–F'03) was with ABB-Scandia, Randers, Denmark, from 1987 to 1988. From 1988 to 1992, he was a Ph.D. Student with Aalborg University, Aalborg, Denmark. He became an Assistant Professor in 1992, Associate Professor in 1996, and Full Professor of power electronics and drives in 1998. His current research interests include power electronics and its applications such as in wind turbines, PV systems, reliability, harmonics and adjustable speed drives.

He has received 17 IEEE Prize Paper Awards, the IEEE PELS Distinguished Service Award in 2009, the EPE-PEMC Council Award in 2010, the IEEE William E. Newell Power Electronics Award 2014 and the Villum Kann Rasmussen Research Award 2014. He was an Editor-in-Chief of the IEEE TRANSACTIONS ON POWER ELECTRONICS from 2006 to 2012. He is nominated in 2014 and 2015 by Thomson Reuters to be between the most 250 cited researchers in Engineering in the world.

Wei Wang (M'13) received her B.S. degree in Automatic Test and Control from Harbin Institute of Technology, Harbin, China, in 1984, her M.S. degree in Electrical Engineering from Harbin Institute of Technology in 1990, and her Ph.D. degree in Mechanical Electronic Engineering from Harbin Institute of Technology in 2002. In 1984, she joined Harbin Institute of Technology, as an Assistant Professor in the Department of Electrical Engineering, where she was an Associate Professor from 1995 to 2003, and where she has been a Professor since 2003.

She current research interests include regenerative energy converter techniques, micro-grid, soft-switching converters, and lighting electronic technology.

Dianguo Xu (M'97–SM'12) received the B.S. degree in Control Engineering from Harbin Engineering University, Harbin, China, in 1982, and the M.S. and Ph.D. degrees in Electrical Engineering from Harbin Institute of Technology (HIT), Harbin, China, in 1984 and 1989 respectively.

In 1984, he joined the Department of Electrical Engineering, HIT as an assistant professor. Since 1994, he has been a professor in the Department of Electrical Engineering, HIT. He was the Dean of School of Electrical Engineering and Automation, HIT from 2000 to 2010. He is now the vice president of HIT. His research interests include renewable energy generation technology, multi-terminal HVDC system based on VSC, power quality mitigation, speed sensorless vector controlled motor drives, high performance PMSM servo system. He published over 600 technical papers.

Prof. Xu is an Associate Editor of the IEEE Transactions on Industrial Electronics and the IEEE Journal of Emerging and Selected Topics in Power Electronics. He also serves as Chairman of IEEE Harbin Section, Director of Lighting Power Supply Committee of CPSS, Vice-director of Electric Automation Committee of CAA, Electrical Control System & Equipment Committee of CES, and Power Electronics Committee of CES.